Journal of Materials Chemistry A

Kinetic Analysis and Alloy Designs for Metal/Metal Fluorides toward High Rate Capability for All-solid-state Fluoride Ion Batteries

Journal:	*Journal of Materials Chemistry A*
Manuscript ID	TA-ART-12-2020-012055.R1
Article Type:	Paper
Date Submitted by the Author:	30-Jan-2021
Complete List of Authors:	Yoshinari, Takahiro; Kyoto University, Graduate School of Human and Environmental Studies Zhang, Datong; Kyoto University, Graduate School of Human and Environmental Studies Yamamoto, Kentaro; Kyoto University, Graduate School of Human and Environmental Studies Kitaguchi, Yuya; Kyoto University, Graduate School of Human and Environmental Studies Ochi, Aika; Kyoto University, Graduate School of Human and Environmental Studies Nakanishi, Koji; Kyoto University, Graduate School of Human and Environmental Studies Miki, Hidenori; Kyoto University, Graduate School of Human and Environmental Studie Nakanishi, Shinji; TOYOTA MOTOR CORPORATION, Battery Research Division Iba, Hideki; Toyota Motor Corporation Higashifuji Research Center Uchiyama, Tomoki; Kyoto University, Human and Environmental Studies Watanabe, Toshiki; Kyoto University, Graduate School of Human and Environmental Studies Matsunaga, Toshiyuki; Kyoto University, Human and Environmental Studies Amezawa, Koji; Tohoku University, IMRAM Uchimoto, Yoshiharu; Kyoto University, Graduate School of Human and Environmental Studies; High Energy Accelerator Research Organisation, Institute of Materials Structure Science

ARTICLE

Kinetic Analysis and Alloy Designs for Metal/Metal Fluorides toward High Rate Capability for All-solid-state Fluoride-ion Batteries

Received 00th January 20xx,
Accepted 00th January 20xx

DOI: 10.1039/x0xx00000x

Takahiro Yoshinari, [a†] Datong Zhang, [a†] Kentaro Yamamoto, [a*] Yuya Kitaguchi, [a] Aika Ochi, [a] Koji Nakanishi, [a] Hidenori Miki, [a,b] Shinji Nakanishi, [b] Hideki Iba, [b] Tomoki Uchiyama, [a] Toshiki Watanabe, [a] Toshiyuki Matsunaga, [a] Koji Amezawa [c] and Yoshiharu Uchimoto [a, d]

New concepts for electrochemical energy storage devices are required to handle the physicochemical energy density limit that Li-ion batteries are approaching. All-solid-state fluoride-ion batteries (FIBs), in which monovalent fluoride anions are employed as charge carriers, are regarded as attractive options, and metallic Cu has been proved to be a promising cathode material. However, the rate capability is currently low and kinetic factors associated with the Cu/CuF2 reaction are not clearly understood, and the rate-determining step has not yet been identified. Herein, we present the kinetic analyses to a Cu thin-film cathode with a phase-boundary-controlled one-dimensional phase transition process via the Kolmogorov-Johnson-Mehl-Avrami equation. Concerning the capacity fading caused by the repeated volume expansion/contraction and the consequent interfacial contact loss, a Cu-Au alloy with reduced lattice mismatch was designed and verified to be efficient to enable fast phase-transition kinetics along with stable cyclabilities, which opens new possibilities in cathode design for all-solid-state FIBs.

Introduction

Electrochemical energy storage devices with high energy density are essential for energy diversification and a sustainable future. [1, 2] Typical Li-ion batteries have dominated the market for over 30 years; [3] however, they are reaching their physicochemical limits, while other intercalation-type alternatives such as Mg-ion, Ca-ion, and Zn-ion batteries are still unable to meet the growing energy and power density requirements. [4] Although multivalent ions can offer high capacities with acceptable voltages, the strong electrostatic interactions between the diffusing multivalent cations and the host anions hinder application to reversible cathodes. [5] All-solid-state fluoride-ion batteries (FIBs) have considerable potential to enable high energy density while being highly safe. [6] As monovalent fluoride ions are employed as anion charge carriers, the possibilities for material designs based on the counter cation are almost limitless and can even include those that involve simple metals or alloys.

All-solid-state FIBs that utilize metal/metal fluoride [7-15] and intercalation oxide [16-19] as electrode materials have been reported in recent decades. Tysonite-type $La_{0.9}Ba_{0.1}F_{2.9}$ is commonly used as a solid electrolyte and is stable in a wide potential range for battery operation. [20] For metal/metal fluoride (M/MF_x) systems, various combinations, for example, those featuring Cu, Co, Ni, Bi, and Sn, [8, 15, 21-28] have been evaluated as candidates with reversible (de)fluorination behaviors, but the reaction mechanisms have not been elucidated thus far. Among the various M/MF_x combinations, Cu/CuF_2 has been proved to be a promising candidate for the cathodes of all-solid-state FIBs, which follow a two-phase-transition reaction pattern upon (de)fluorination, according to several reports and our recent study. [21] Nevertheless, there are some essential points that remain undetermined. As we have emphasized, [21] investigations on kinetics are necessary to identify the rate-determining step of the Cu/CuF_2 phase transition; meanwhile the enormous volumetric changes upon (de)fluorination of Cu/CuF_2 (~195.6 %) must be addressed, or the severe lattice mismatch on the Cu/CuF_2 interface will further worsen the structural integrity.

Herein, we report a kinetic analysis for Cu/CuF_2 cathode with a phase-boundary-controlled one-dimensional phase transition process, along with its rational design that involved alloying with the electrochemically inactive Au, which remarkably enhanced the overall performance. The large lattice mismatch between Cu and CuF_2 was effectively buffered by introducing an intermediate Cu_3Au alloy, which led to high rate capability as well as long cycle life. This study also showed that appropriate suppression of the lattice strain within the phase boundary can be crucial for material design for all-solid-state FIBs.

[a.] *Graduate School of Human and Environmental Studies, Kyoto University, Yoshida-nihonmatsu-cho, Sakyo, Kyoto 606-8501, Japan.*
[b.] *Battery Research Div., Higashifuji Technical Center, Toyota Motor Corporation, 1200 Mishuku, Susono, Shizuoka 410-1193, Japan.*
[c.] *Institute of Multidisciplinary Research for Advanced Materials, Tohoku University, 2-1-1 Katahira, Aoba, Sendai, Miyagi 980-8577, Japan.*
[d.] *Institute of Materials Structure Science, High Energy Accelerator Research Organization (KEK), Tsukuba 305-0801, Japan*
† These authors contributed equally to this work.

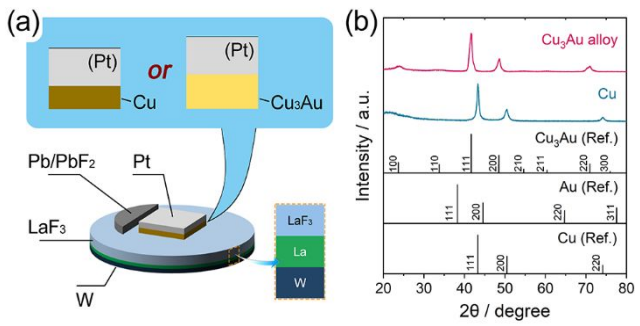

Figure 1. (a) Schematic illustrations of thin-film cells that employ Cu and Cu_3Au as working electrodes. (b) X-ray diffraction (XRD) patterns of as-deposited Cu and Cu_3Au materials.

Results and Discussion

Phases of as-prepared Cu and Cu_3Au films

Phases of as-prepared Cu and Cu_3Au films. A typical thin-film model cell was fabricated as shown in Figure 1a, with a Pb/PbF_2 reference electrode (R.E.) constructed for accurate evaluation of the electrochemical properties. To gain further understanding of the kinetics of Cu/CuF_2 systems, Cu thin films of two thicknesses, 2.3 and 10 nm, were used in this study. For the alloying, stoichiometric amounts of Au corresponding to thicknesses of 1.1 and 4.8 nm, respectively, were deposited. The X-ray diffraction (XRD) results (Figure 1b) of both the as-prepared Cu and Cu_3Au films corresponded well with reference patterns ($Fm\bar{3}m$ and $Pm\bar{3}m$, respectively), and no separated phase such as Cu and Au was observed in the Cu_3Au alloy. Although the introduction of Au atoms changed the overall symmetry of the lattice and led to new diffractions that do not appear for unalloyed Cu (such as (100), (110), (210), (211), and (300)), it is still clear that the main diffraction peaks (i.e., (111), (200), and (220)) shifted toward lower angles. These shifts are reasonable because Cu_3Au possesses larger lattice parameters ($a = b = c = 3.74$ Å) [29] than those of Cu metal ($a = b = c = 3.608$ Å) [30] owing to the larger atomic radius [31] of Au (approximately 144 pm) than that of Cu (approximately 128 pm). These parameters are consistent with our calculated lattice parameters of $a = b = c = 3.782$ Å for Cu_3Au and $a = b = c = 3.615$ Å for Cu.

Kinetic analysis of the Cu/CuF_2 system

According to our previous study, [21] unalloyed Cu (2.3 nm) can deliver a high initial reversible capacity of 670.5 mAh g^{-1} at 84.3 mA g^{-1} during galvanostatic charge–discharge, upon which the direct two-phase-transition between Cu and CuF_2 phases was investigated, whereas the rate-determining step of the fluorination could not be identified clearly. In the mass/electron transfer process at the cathode side, there are three typical transfer steps, namely (i) F^- transfer inside the CuF_2 bulk, (ii) F^- transfer across the Cu/CuF_2 phase boundary, and (iii) electron transfer toward the Pt current collector via Cu, as shown in Figure 2a. As they are outstanding electronic conductors, electron transfer along Cu and Pt could be regarded as unconstrained; thus, step (iii) cannot possibly be the rate-determining step. Steps (i) and (ii), which actually correspond to F^- diffusions inside the CuF_2 bulk and phase boundary movements, respectively, were evaluated to determine the phase transition mechanism [32-37] via Kolmogorov-Johnson-Mehl-Avrami (KJMA) analysis.

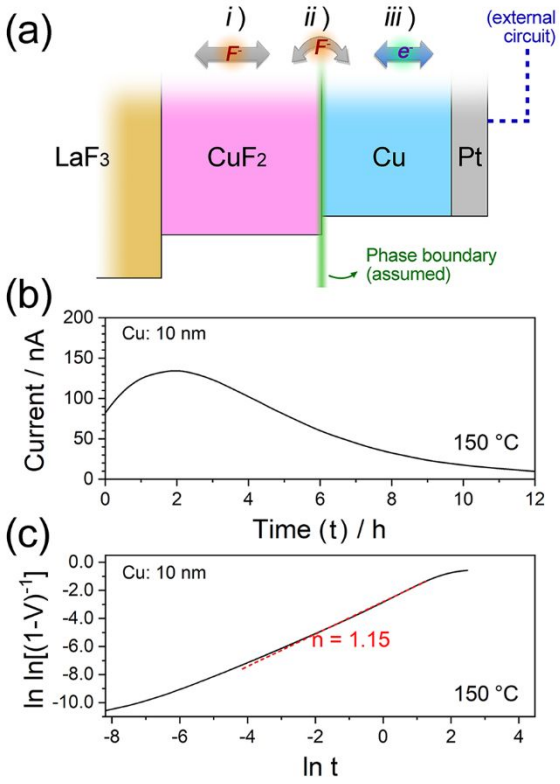

Figure 2. (a) Schematic illustrations of three possible rate-determining steps in two-phase transition process for Cu/CuF_2 system. (b) Current response caused by potential step from 0.68 to 0.66 V vs. Pb/PbF_2 after charging to 1.25 V vs. Pb/PbF_2 at 150 °C. (c) Avrami plot obtained following the potential step treatment. The dashed red line represents the linear fitting result for the Avrami exponent, *n*.

For the two-phase transition, the volume fraction of a new phase (*V*) was expressed as a function of reaction time (t) using equation (1),

$$V = 1 - \exp\left(-kt^n\right) \quad (1)$$

where k is the rate constant of the phase transition and *n* is the Avrami exponent. Equation (1) can be rearranged to equation (2).

$$\ln\ln\left[1/(1-V)\right] = n\ln t + \ln k. \quad (2)$$

The slope of the ln ln [1/(1 − *V*)] vs. ln *t* plot gives the Avrami exponent, which is based on three components, as shown in equation (3),

$$n = a + bc \quad (3)$$

where a is the nucleation index (a = 0 for a nucleation rate of 0, 0 < a < 1 for decreasing nucleation rates, a = 1 for constant nucleation, and a > 1 for increasing nucleation rates), b is the dimension of growth (b = 1, 2, or 3 for one-dimensional (1D), two-dimensional (2D), and three-dimensional (3D) growth, respectively), and c is a growth index that is dependent on the rate-determining step of the transformation (c = 1 for phase-boundary-controlled growth and c = 1/2 for diffusion-controlled growth). The nucleation index, a, governs the time (t) dependence of the number of nuclei per unit volume of an untransformed material (N) [38, 39] (equation (4)):

$$N \propto t^a \quad (4)$$

In the case of the Cu/CuF_2 reaction, potential-step chronoamperometry was used to induce the phase transition for KJMA analysis (Figure 2b), which was carried out after the materials were fully charged to 1.25 V and using potential steps of 0.68 to 0.66 V (the reaction potential of Cu/CuF_2). The current increased for 2 h and then decreased gradually, corresponding to the nucleation and growth processes. [40] The volume fraction (V) could be obtained from the state of charge (SOC). The Avrami plot was obtained when the correlation of ln ln [1/(1−V)] vs. ln t was established and is shown in Figure 2c. The Avrami exponent was n = 1.15, which could be interpreted as being due to a phase-boundary-controlled 1D phase transition with decreasing nucleation rate (a = 0.15, b = 1, and c = 1). For the parameter c, the diffusion-controlled growth (c = 1/2) would be kinetically unfavorable. The high strain energy caused by lattice mismatch on the Cu/CuF_2 interface do not vary throughout the whole reaction; while the diffusion-controlled growth normally follows a parabolic law, ($r = A(Dt)^{0.5}$, where r is the particle radius) [41] which indicates the growth was ultrafast at first and gradually slowed down. Consequently, the model of the phase-boundary-controlled 1D phase transition should be the plausible interpretation. Also, the decreasing nucleation rate (a = 0.15) is in good agreement with the nucleation behavior considering the strong correlations between the phase boundary movement (accompanying with the nucleation and growth) and phase transition kinetics.

Effect of alloying on Cu material

The confirmation of F^- transfer across the phase boundary being the rate-determining step led us to concentrate more on the intrinsic large lattice mismatch at the two-phase interfaces that hindered overall battery performance. Therefore, an intermediate Cu_3Au Cu-Au alloy that buffered the large lattice volume differences was designed and evaluated as the cathode material for all-solid-state FIBs; the electrochemical properties before and after alloying were investigated. The Au component was considered as being electrochemically inactive owing to the high fluorination potential of Au; [42] thus, the actual specific capacity was calculated using only the mass of Cu (theoretical capacity of ~843 mAh g^{-1}), and the 1 C rate was defined as 843 mA g^{-1} for both Cu and Cu_3Au. For the evaluation of cyclability, Cu with a thickness of 2.3 nm was utilized to create a more ideal reaction environment. For comparing the rate capabilities, which would be significantly affected by kinetic factors, Cu with a thickness of 10 nm was utilized because a larger thickness would amplify the weakness of the 1D phase transition model; therefore, the enhancements of the rate capabilities due to alloying under such unfavorable conditions would be more convincing. Moreover, all electrochemical tests were carried out at 150 °C for adequate ionic conductivity of LaF_3 substrates unless stated otherwise. Figure 3a shows that the Cu and Cu_3Au cathodes gave initial reversible capacities of 670.5 and 606.9 mAh g^{-1}, respectively, at C/10, which may be ascribed to the disturbance to the atoms rearrangement of Cu/CuF_2 process due to the presence of Au atoms, leading to a slight decrease in the initial capacity. However, cycle deterioration for Cu_3Au was well suppressed; after 20 cycles, the capacity of Cu_3Au was almost twice that of Cu (469.6 vs. 253.8 mAh g^{-1}) and the corresponding capacity retentions were 77.4% and 37.9% for Cu_3Au and Cu, respectively. In addition, the enhancements of the rate capabilities were impressive, as superior performances were achieved by Cu_3Au at all rates except for the lowest rate of C/50. From rates of C/50 to C/5, the capacity retentions of Cu and Cu_3Au were 48.5% and 81.9%, respectively. The charge–discharge profiles of Cu and Cu_3Au at C/50 and C/5 are shown in Figure 3b. Clearly, the polarization of Cu_3Au is lower than that of Cu, and the identical charge–discharge potentials at C/50 indicated that Cu and Cu_3Au have

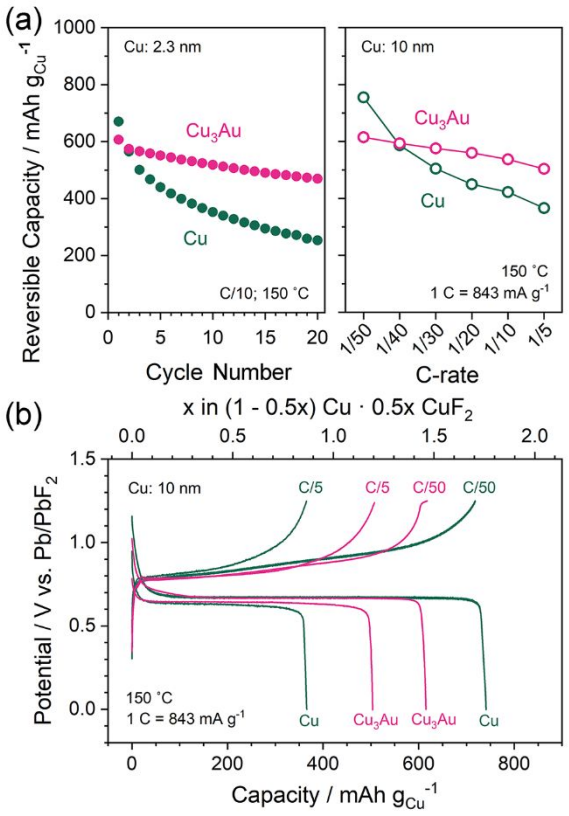

Figure 3. (a) Cyclability (left) and rate performance (right) of Cu and Cu_3Au at 150 °C. (b) Galvanostatic charge–discharge curves of Cu and Cu_3Au at C/50 and C/5 at 150 °C.

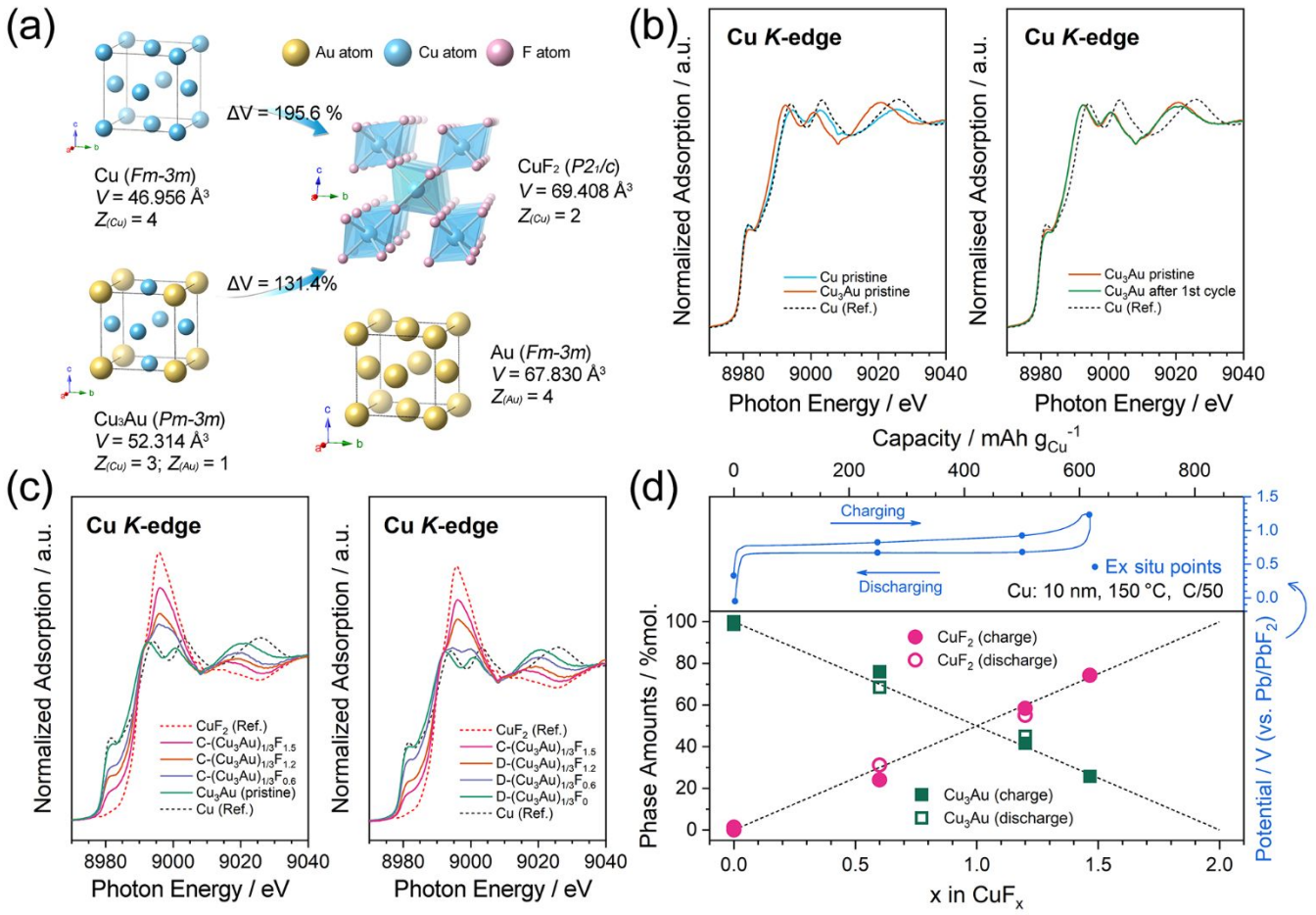

Figure 4. (a) Crystallographic structures and parameters of Cu, Au, Cu_3Au, and CuF_2. Charge compensation mechanism of Cu-Au alloy. [29, 30, 43, 44] (b) Cu K-edge X-ray adsorption spectroscopy (XAS) patterns of as-deposited Cu and Cu_3Au (left) and as-deposited and cycled Cu_3Au (right). (c) Ex situ Cu K-edge XAS patterns of Cu_3Au upon charging (left) and discharging (right). (d) Phase amounts for Cu_3Au and CuF_2 upon charging/discharging; dashed lines connect (0,0) with (2,100) and (0,100) with (2,0), that is, the ideal phase amount changes of a two-phase transition.

the same redox systems, that is, the Cu/CuF_2 redox system, which is consistent with our hypothesis that Au is electrochemically inactive. Therefore, reduction of the lattice mismatch through alloying was verified to be effective for achieving high rate performance and long cycle life owing to a smooth phase transition.

Enhancement mechanisms and charge compensation behaviours

The related crystallographic structure is presented in Figure 4a (some information is also shown in Figure 1c). The Cu_3Au had a similar structure to that of metallic Cu, with the corner atoms in the Cu lattice being replaced by Au. [29] Since an Au atom possesses a larger atomic radius than that of Cu, substitution of the corner Cu atoms with Au atoms changed the face-centered cubic ($Fm\bar{3}m$ space group) symmetry to primitive cubic ($Pm\bar{3}m$ space group) symmetry, increasing the lattice volume (V_L). In brief, unalloyed Cu possesses four Cu atoms per lattice with V_L = 46.956 Å³, while Cu_3Au possesses three Cu atoms and one Au atom per lattice with V_L = 52.314 Å³. [29, 30] Note that the Au component was treated as being electrochemically inactive and the fully charged products of Cu_3Au were the same as those of unalloyed Cu metal, that is, CuF_2, which possesses two Cu atoms per lattice [43] with VL = 69.408 Å³, was produced instead of CuF_2 + AuF_3 or some $(Cu_3Au)F_x$ compound. Based on these reaction routes, the respective volumetric changes of Cu and Cu_3Au after fluorination can be calculated as follows. The volumes were the average values for each Cu atom, considering the different number of Cu atoms in the above lattices.

For converting Cu to CuF_2, the charging reaction is,

$$Cu + 2F^- \rightarrow CuF_2 + 2e^-$$

where the initial volume is V_L(Cu)/4 = 11.739 Å³ and the final volume is V_L(CuF_2)/2 = 34.704 Å³; thus, the corresponding volume change was 195.6%, which is consistent with the values in previous reports. [25]

Similarly, for the conversion of Cu_3Au to CuF_2, the charging reaction is,

$$Cu_3Au + 6F^- \rightarrow 3CuF_2 + Au + 6e^-$$

where the initial volume is V_L(Cu_3Au) = 52.314 Å³ and the final volume is 3V_L(CuF_2)/2 + V_L(Au)/4 = 121.07 Å³ (Au: $Fm\bar{3}m$, four Au atoms per lattice, V_L = 67.830 Å³, Figure 4a); [44] thus, the corresponding volume change was 131.4%. Clearly, the substitution of Au reduced the severe volumetric changes caused by the (de)fluorination of Cu, resulting in a limited

lattice mismatch at the Cu/CuF_2 phase boundary. The success of lattice mismatch buffering was owing to the high structural similarity between Cu_3Au and Cu lattices and the electrochemical inactivity of Au in the selected potential range. It is believed that such strategy is widely appliable for many similar alloy systems. For example, in the circumstance of employing Cu/CuF_2 redox, there is also a similar Cu_3Pt intermediate compound in Cu-Pt alloy system with an electrochemically inactive Pt species; therefore, the buffering effect shall also be achievable in Cu-Pt system.

The phase transition and charge compensation mechanism of the Cu_3Au cathode were studied using ex situ X-ray adsorption near-edge spectroscopy (XANES, Figure 4b–4d). The spectrum of pristine Cu_3Au was shifted slightly toward lower energy than that of pristine Cu, which is in good agreement with a previous report. [45] Note that the Cu_3Au spectra before and after cycling overlapped completely, suggesting that Cu_3Au was regenerated after the phase transition to CuF_2 and Au. As shown in Figure 4c, upon charge–discharge, the intermediate spectra of Cu_3Au with various fluoride-ion contents changed between the Cu_3Au and CuF_2 reference spectra with a pair of isosbestic points, which indicates two-phase-transition behavior identical to that of Cu/CuF_2 systems, as we reported recently. [21] The results of linear fitting for the Cu_3Au and CuF_2 phase amounts also indicated the two-phase nature of Cu_3Au upon electrochemical (de)fluorination (Figure 4d).

Kinetic analysis of the Cu_3Au/CuF_2 system

The phase transition kinetics were investigated quantitatively. With a 1D phase transition, the ratio between the charges at a certain time ($t = t'$) and at the final time ($t = \infty$) is equivalent to the ratio between the thicknesses of a new phase and the entire electrode, [46, 47] as shown in equation (5):

$$Q_{t'}/Q_{\infty} = [l - (l - \xi)]/l \quad (5)$$

where $Q_{t'}$ is the charge at time t', Q_{∞} is the total charge required to complete the phase transition, ξ is the thickness of a new phase, and l is the thickness of the entire electrode (i.e., the thickness at the end of the phase transition). Thus, ξ can be presented as a function of t. According to the Wagner model for diffusion in a binary system containing a phase boundary, [48] phase boundaries move linearly with $t'^{1/2}$, as shown in equation (6):

$$\xi = 2\gamma(Dt')^{1/2} = k't'^{1/2} \quad (6)$$

where γ is a dimensionless parameter, D is the diffusion coefficient for a new phase, and k' is the phase boundary rate constant. Therefore, the values of k' can be acquired from the slope of the ξ vs. $t'^{1/2}$ lines.

Potential-step chronoamperometry was again used to induce the phase transition in the Cu and Cu_3Au cathodes (Figure 5a) at 25 °C for quantitative comparison with highly commercialized Li-ion battery materials. Correspondingly, a potential step of 0.76 to 0 V was used instead, considering the larger polarization at a mild temperature. The Cu_3Au cathode showed typical nucleation and growth behaviour at a high current and fast decline to zero current compared with Cu. The

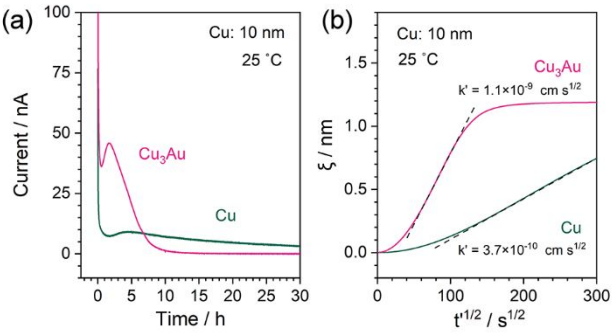

Figure 5. Analyses of phase-boundary movements of two-phase-transition Cu and Cu_3Au. (a) Results of potential-step chronoamperometry from 0.76 to 0 V at 25 °C after charging to 1.25 V vs. Pb/PbF_2 at 150 °C. (b) Plots of ξ vs. $t'^{1/2}$ based on Wagner model.

correlations between ξ and $t'^{1/2}$ were established as shown in Figure 5b. Linear fitting was conducted during the nucleation process, and the electric double layer capacity at a very early stage of the reaction was excluded. The obtained phase boundary rate constant for Cu_3Au was 1.1×10^{-9} cm $s^{1/2}$, which is three times higher than the value of 3.7×10^{-10} cm $s^{1/2}$ for Cu.

Although alloying enhanced the phase transition kinetics, this value was still four orders of magnitude lower than that of $LiFePO_4$, [49] the typical counterpart in the lithium-ion battery field with a two-phase-transition mechanism. Hindered by the inferior kinetics, Cu material could hardly exhibit comparable rate capability as LIBs even after being optimized by Cu-Au alloy strategy. This result indicated the large difficulties for all-solid-state FIBs that required to be overcome. Moreover, the lack of suitable solid electrolyte also lowered the overall performance of all-solid-state FIBs; therefore, developments of solid electrolytes with high conductivity at room temperature are strongly appealed as well.

Conclusions

Cu and Cu_3Au thin-film models were utilized for the fabrication of cathode materials for all-solid-state FIBs. A one-dimensional phase transition limited by phase boundary movement was determined using KJMA analysis. An alloying strategy was employed to address the large lattice mismatch between Cu and CuF_2, which has led to enhanced battery performances. Cu_3Au enabled the buffering of the volumetric differences, thus reducing the lattice strain at the phase boundary, and showed a high rate performance and long cycle life than that of Cu. A highly reversible two-phase reaction between Cu_3Au and CuF_2 was also observed. Although alloying was effective in enhancing the overall performance, the phase transition rate constant calculated using the Wagner model was still much lower than that of commercialized $LiFePO_4$. The elimination of the bottleneck by alloying will lead to new strategies for further development of metal-based electrodes for all-solid-state FIBs.

Experimental Section

Battery preparation

Table 1. RF sputtering conditions

Element	Thickness/nm	Power/W	Atmosphere	Pressure/Pa
Cu	2.3 or 10	50	Ar	1.0
Pb	1000	50	Ar	1.0
Au	1.1 or 4.8	50	Ar	1.0
W	50	120	Ar	1.0
Pt	50	50	Ar	1.0

A thin-film all-solid-state FIB cell was fabricated on a LaF_3 solid electrolyte using the radio frequency (RF) magnetron sputtering method. Single-crystalline LaF_3 substrate (Pier Optics, Japan) with a thickness of 0.5 mm was used as the solid electrolyte. The surface of the cathode side of the substrate was mirror-polished and its roughness was evaluated through atomic force microscopy (AFM) images. The same surface was processed by reverse sputtering with argon plasma and annealed for 1 h at 300 °C in a NF_3 gas atmosphere. The ionic conductivity of the solid electrolyte was 1.1×10^{-3} S cm^{-1} at 150 °C. Afterwards, Cu and Pb thin films were deposited on the substrate and used as the working and reference electrodes, respectively. The Cu_3Au alloy thin-film electrode was prepared by annealing at 300 °C for 1 h after the deposition of Au onto Cu. The thicknesses of both electrodes were detected in real-time using a quartz crystal microbalance (QCM) installed in the sputtering chamber. La metal could be produced from LaF_3 and was used as the counter electrode. For the current collectors, Pt and W were deposited on the sides of the working and counter electrodes, respectively. These metals were selected because they can remain intact during the electrochemical measurements. The sputtering conditions are listed in **Table 1**. Finally, the as-deposited Pb was pre-fluorinated to PbF_2 for a stable reference potential, as La being simultaneously produced from LaF_3 at the counter electrode. The preparation procedures, AFM images, characterization of the LaF_3 substrates, verifications of film thickness, and pre-fluorination of the Pb reference electrode can be found in our previous work. [21]

Characterizations

XRD measurements. The thin-film electrodes deposited on a synthetic silica glass substrate were examined via XRD using an Ultima IV (Rigaku, Japan) with Cu *Kα* radiation. The X-ray tube current and voltage were 40 mA and 40 kV, respectively. The data were obtained with a sample-stage rotation speed of 120 rpm and scanning rates of 0.1°/min.

Charge–discharge measurements. Galvanostatic charge–discharge cycling was performed at various C-rates (1 C = 843 mA g^{-1}) in a potential range of 0 to 1.25 V vs. Pb/PbF_2 at 150 and 25 °C using a PARSTAT MC2000 (Princeton Applied Research, USA).

XAS measurements. The samples were prepared through electrochemical (de)fluorination at particular fluorine contents in (1 - 0.5x) M □ 0.5x MF_2 (M = Cu or $(Cu_3Au)_{1/3}$, $0 \le x \le 2$). They were transferred from an argon-filled glovebox to the analysis chamber in sealed containers without air exposure. Cu *K*-edge XANES measurements were performed at BL01B1 and BL37XU (SPring-8, Japan). The absorption spectra were collected in partial fluorescence yield (PFY) mode using a 19-element solid-state detector.

Conflicts of interest

There are no conflicts to declare.

Acknowledgements

This work was supported by JST-Mirai Program Grant Number JPMJMI18E2, Japan. Synchrotron radiation experiments were performed at beam lines BL37SU and BL01B1 of SPring-8 with the approval of the Japan Synchrotron Radiation Research Institute (JASRI) (Proposal number 2016B1021, 2017B1038, 2019B1014 and 2019B1016).

Contributions of Co-authors

T. Yoshinari and D. Zhang played the following role: Conceptualization, Investigation (performing the electrochemical experiments, data collection about synchrotron X-ray absorption spectroscopy), Data Curation, Formal analysis (computational techniques to analyse synchrotron X-ray absorption spectroscopy data), Validation, Writing - Original Draft. Y. Kitaguchi and A. Ochi conducted the experimental work of the electrochemical experiments and data collection about synchrotron X-ray absorption spectroscopy. K. Nakanishi and T. Watanabe prepared the measurement environment of X-ray absorption spectroscopy. T. Uchiyama and T. Matsunaga measured the synchrotron X-ray absorption spectroscopy and X-ray diffraction. K. Amezawa performed the formal analysis. H. Miki, S. Nakanishi, and H. Iba analysed the electrochemical data and Validation. Y. Uchimoto played the following role: Conceptualization, Funding acquisition, Resources, Writing - Review & Editing. The ideas and experiments were conceived, planned, and analysed by all co-authors under the supervision of K. Yamamoto. All authors have given approval to the final version of the manuscript.

References

1 C. P. Grey and J. M. Tarascon, *Nat. Mater.*, 2017, **16**, 45-56.
2 S. Chu, Y. Cui and N. Liu, *Nat. Mater.*, 2017, **16**, 16-22.
3 J. Janek and W. G. Zeier, *Nat. Energy*, 2016, **1**, 16141.
4 P. Canepa, G. S. Gautam, D. C. Hannah, R. Malik, M. Liu, K. G. Gallagher, K. A. Persson and G. Ceder, *Chem. Rev.*, 2017, **117**, 4287-4341.
5 E. Levi, M. D. Levi, O. Chasid and D. Aurbach, *J. Electroceram.*, 2007, **22**, 13-19.
6 F. Gschwind, G. Rodriguez-Garcia, D. J. S. Sandbeck, A. Gross, M. Weil, M. Fichtner and N. Hörmann, *J. Fluorine Chem.*, 2016, **182**, 76-90.
7 M. A. Reddy and M. Fichtner, *J. Mater. Chem.*, 2011, **21**, 17059-17062.

8 C. Rongeat, M. A. Reddy, R. Witter and M. Fichtner, *J Phys. Chem. C*, 2013, **117**, 4943-4950.
9 C. Rongeat, M. A. Reddy, T. Diemant, R. J. Behm and M. Fichtner, *J. Mater. Chem. A*, 2014, **2**, 20861-20872.
10 A. Grenier, A. G. P. Gutierrez, H. Groult and D. Dambournet, *J. Fluorine Chem.*, 2016, **191**, 23-28.
11 M. H. Fawey, V. S. K. Chakravadhanula, M. A. Reddy, C. Rongeat, T. Scherer, H. Hahn, M. Fichtner and C. Kubel, *Microsc. Res. Tech.*, 2016, **79**, 615-624.
12 A. Grenier, A. G. Porras-Gutierrez, H. Groult, K. A. Beyer, O. J. Borkiewicz, K. W. Chapman and D. Dambournet, *J. Mater. Chem. A*, 2017, **5**, 15700-15705.
13 D. T. Thieu, M. Hammad, H. Bhatia, T. Diemant, V. S. K. Chakravadhanula, R. J. Behm, C. Kubel and M. Fichtner, *Adv. Funct. Mater.*, 2017, **27**.
14 L. Zhang, M. A. Reddy, P. Gao, T. Diemant, R. J. Behm and M. Fichtner, *J. Solid State Electrochem.*, 2017, **21**, 1243-1251.
15 L. Zhang, M. A. Reddy and M. Fichtner, *J. Solid State Electrochem.*, 2018, **22**, 997-1006.
16 O. Clemens, C. Rongeat, M. A. Reddy, A. Giehr, M. Fichtner and H. Hahn, *Dalton Trans.*, 2014, **43**, 15771-15778.
17 M. A. Nowroozi, K. Wissel, J. Rohrer, A. R. Munnangi and O. Clemens, *Chem. Mater.*, 2017, **29**, 3441-3453.
18 M. A. Nowroozi, S. Ivlev, J. Rohrer and O. Clemens, *J. Mater. Chem. A*, 2018, **6**, 4658-4669.
19 M. A. Nowroozi, B. de Laune and O. Clemens, *ChemistryOpen*, 2018, **7**, 617-623.
20 A. Grenier, A. G. Porras-Gutierrez, M. Body, C. Legein, F. Chretien, E. Raymundo-Pinero, M. Dolle, H. Groult and D. Dambournet, *J. Phys. Chem. C*, 2017, **121**, 24962-24970.
21 D. Zhang, K. Yamamoto, A. Ochi, Y. Wang, T. Yoshinari, K. Nakanishi, H. Nakano, H. Miki, S. Nakanishi, H. Iba, T. Uchiyama, T. Watanabe, K. Amezawa and Y. Uchimoto, *J. Mater. Chem. A*, 2020, in press. https://doi.org/10.1039/D0TA08824B
22 M. Anji Reddy and M. Fichtner, *J. Mater. Chem.*, 2011, **21**, 17059-17062.
23 C. Rongeat, M. Anji Reddy, T. Diemant, R. J. Behm and M. Fichtner, *J. Mater. Chem. A*, 2014, **2**, 20861-20872.
24 K.-i. Okazaki, Y. Uchimoto, T. Abe and Z. Ogumi, *ACS Energy Lett.*, 2017, **2**, 1460-1464.
25 L. Zhang, M. A. Reddy and M. Fichtner, *J. Solid State Electrochem.*, 2017, **22**, 997-1006.
26 V. K. Davis, C. M. Bates, K. Omichi, B. M. Savoie, N. Momcilovic, Q. Xu, W. J. Wolf, M. A. Webb, K. J. Billings, N. H. Chou, S. Alayoglu, R. K. McKenney, I. M. Darolles, N. G. Nair, A. Hightower, D. Rosenberg, M. Ahmed, C. J. Brooks, T. F. Miller, 3rd, R. H. Grubbs and S. C. Jones, *Science*, 2018, **362**, 1144-1148.
27 I. Mohammad, R. Witter, M. Fichtner and M. A. Reddy, *ACS Appl. Energy Mater.*, 2019, **2**, 1553-1562.
28 M. H. Fawey, V. S. K. Chakravadhanula, A. R. Munnangi, C. Rongeat, H. Hahn, M. Fichtner and C. Kübel, *J. Power Sources*, 2020, **466**.
29 H. D. Megaw, in Crystal structure: a working approach, Philadelphia, 1973, pp. 89-90.
30 E. A. Owen and E. L. Yates, *Philos. Mag.*, 1933, **15**, 472-488.
31 N. Greenwood, Chemistry of the Elements, Elsevier Science & Technology Books, 1996.
32 M. Avrami, *J. Chem. Phys.*, 1939, **7**, 1103-1112.
33 M. Avrami, *J. Chem. Phys.*, 1940, **8**, 212-224.
34 M. Avrami, *J. Chem. Phys.*, 1941, **9**, 177-184.
35 B. Johnson and R. Mehl, *Trans. Am. Inst. Min. Metall. Eng.*, 1939, **135**, 416-422.
36 J. L. Allen, T. R. Jow and J. Wolfenstine, *Chem. Mater.*, 2007, 19, 2108-2111.
37 Y. Orikasa, T. Maeda, Y. Koyama, T. Minato, H. Murayama, K. Fukuda, H. Tanida, H. Arai, E. Matsubara, Y. Uchimoto and Z. Ogumi, *J. Electrochem. Soc.*, 2013, **160**, A3061-A3065.
38 S. Ranganathan and M. Vonheimendahl, *J. Mater. Sci.*, 1981, **16**, 2401-2404.
39 G. Ruitenberg, A. K. Petford-Long and R. C. Doole, *J. Appl. Phys.*, 2002, **92**, 3116-3123.
40 G. Oyama, Y. Yamada, R.-i. Natsui, S.-i. Nishimura and A. Yamada, *J. Phys. Chem. C*, 2012, 116, 7306-7311.
41 S. Ranganathan and M. Von Heimendahl, *J. Mater. Sci.*, 1981, **16**, 2401-2404.
42 K. Motohashi, T. Nakamura, Y. Kimura, Y. Uchimoto and K. Amezawa, *Solid State Ionics*, 2019, **338**, 113-120.
43 P. Fischer, W. Hälg, D. Schwarzenbach and H. Gamsjäger, *J. Phys. Chem. Solids*, 1974, **35**, 1683-1689.
44 R. W. G. Wyckoff, in Crystal structures, 2nd edition., Interscience Publishers, 1963, vol. 1, pp. 7-83.
45 M. Kuhn and T. K. Sham, *Phys. Rev. B Condens. Matter*, 1994, **49**, 1647-1661.
46 M. D. Levi, E. Markevich and D. Aurbach, *Electrochim. Acta*, 2005, **51**, 98-110.
47 M. D. Levi and D. Aurbach, *J. Solid State Electrochem.*, 2007, **11**, 1031-1042.
48 A. Funabiki, M. Inaba, T. Abe and Z. Ogumi, *J. Electrochem. Soc.*, 1999, **146**, 2443-2448.
49 J. Hong, C. S. Wang and U. Kasavajjula, *J. Power Sources*, 2006, **162**, 1289-1296.